

Measurement of Stimulated Raman Side-Scattering Predominance and Energetic Importance in the Compression Stage of the Double-Cone Ignition Approach to Inertial Confinement Fusion

K. Glize,^{1,2,*} X. Zhao,^{1,2,*} Y. H. Zhang,^{3,2} C. W. Lian,⁴ S. Tan,⁵ F. Y. Wu,^{1,2}
C. Z. Xiao,⁵ R. Yan,⁴ Z. Zhang,^{3,2,6} X. H. Yuan,^{1,2,†} and J. Zhang^{1,2,3,†}

¹*Key Laboratory for Laser Plasmas (MoE) and School of Physics and Astronomy, Shanghai Jiao Tong University, Shanghai 200240, China*

²*Collaborative Innovation Center of IFSA (CICIFSA), Shanghai Jiao Tong University, Shanghai 200240, China*

³*Beijing National Laboratory for Condensed Matter Physics, Institute of Physics, Chinese Academy of Sciences, Beijing 100190, China*

⁴*Key Laboratory of Basic Plasma Physics and Department of Engineering and Applied Physics, University of Science and Technology of China, Hefei 230026, China*

⁵*Key Laboratory for Micro-/Nano-Optoelectronic Devices of Ministry of Education, School of Physics and Electronics, Hunan University, Changsha, 410082, China*

⁶*Songshan Lake Materials Laboratory, Dongguan, Guangdong 523808, China*

Due to its particular geometry, stimulated Raman side-scattering (SRSS) drives scattered light emission at non-conventional directions, leading to scarce and complex experimental observations. Experimental campaigns at the SG-II UP facility have measured the scattered light driven by SRSS over a wide range of angles, showing an emission at large polar angles, sensitive to the plasma profile and laser polarization. Furthermore, direct comparison with back-scattering measurement has evidenced SRSS as the dominant Raman scattering process in the compression stage, leading to the scattering loss of about 5% of the total laser energy. The predominance of SRSS was confirmed by 2D particle-in-cell simulations, and its angular spread has been corroborated by ray-tracing simulations. The main implication is that a complete characterization of the SRS instability and an accurate measurement of the energy losses require the collection of the scattered light in a broad range of directions. Otherwise, spatially limited measurement could lead to an underestimation of the energetic importance of stimulated Raman scattering.

In inertial confinement fusion (ICF) experiments [1], one of the main obstacles that prevents the implosion from reaching the required conditions to obtain ignition of the fuel are the laser-plasma instabilities (LPIs) [2], consisting of non-linear couplings of the laser driver beam with plasma modes. Stimulated Raman scattering (SRS) is a three-wave coupling resonantly driving an electron plasma wave (EPW) [3]. This process leads to the scattering of a part of the incident laser reducing the energy coupling, and generation of a hot electron population that can preheat the fuel core. This instability is of primary concern in most of the ICF schemes, such as Indirect-Drive [4–6], Direct-Drive [7, 8] or Shock Ignition [9–12]. Stimulated Raman side-scattering (SRSS) is a particular SRS geometry in which the scattered light is emitted perpendicular to the density gradient, enabling an absolute growth (exponential growth in time at a localised spatial position) at density lower than $n_c/4$, where n_c is the critical density. Despite extensive theoretical investigations in the late 70s [13–15], most of the interest has been focused on stimulated Raman back-scattering (SRBS) [5], due to the experimental complexity to measure SRSS and the largest SRS growth rate for the backward geometry. Recently, there has been a renewed interest due to observations of SRSS on several planar experiments [7, 8, 10, 16, 17], either from single beam interaction, or by multiple beams [18]. Multi-beam processes

happen when the laser beams are sharing a common symmetry axis enabling to drive a shared daughter wave, being either an EPW [19] or a scattered wave [16, 17]. These experimental observations have led to the development of a more complete analytical description of the SRSS, accounting for the convective nature (finite spatial amplification while propagating through the resonant region) of the instability near the turning point, in order to explain the SRSS growth in region below the absolute threshold [20]. It highlighted that ICF experiments are prone to being SRSS unstable as the instability can extend to lower densities in the convective regime due to the large dimensions of the interaction, namely long density scale-length, large laser focal spot and high temperature. Therefore a complete understanding of this detrimental process is imperative as leading to additional laser energy coupling loss and hot electron generation. However, experimental observations have been restricted to a limited number of directions since ICF laser facilities are usually not designed to measure SRS in directions other than back-scattering. Thus, comprehensive measurements of this mechanism and related losses are still not available. In order to improve the overall characterisation of SRS at non-typical angles, crucial new diagnostics are currently being implemented in order to provide further observations at additional angles of observations [21].

In this Letter, we present, up to our knowledge, the

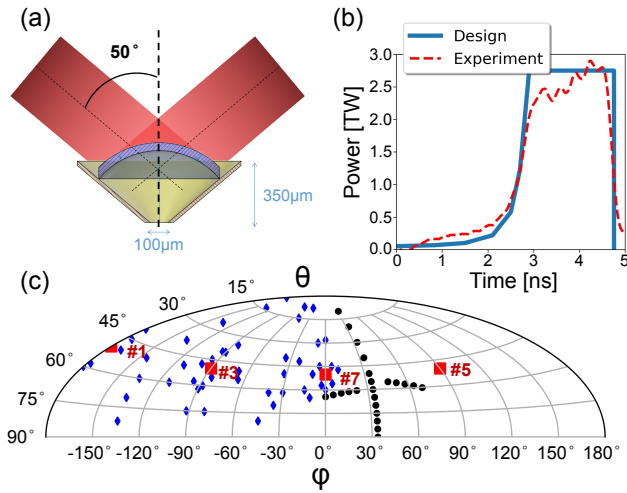


Figure 1. (a) Schematic of the irradiation geometry on the conical target. (b) Pulse shape of the overlapped power delivered on target, both design (blue) and experimental (dashed red). (c) Spherical coordinate map depicting the positions of the laser beams (red squares), the ARSDS fibers (black dots) and the additional 50 fibers (blue diamonds).

first highly-resolved 2D angular measurement of SRS in ICF experiment. These measurements have been obtained in the context of the Double-Cone Ignition (DCI) scheme [22], a newly proposed approach to Direct-Drive (DD) ignition [23], in which the compression and ignition stages are separated. During the preliminary experimental campaigns, focused on the compression stage at low laser intensity, a new diagnostic has been designed and implemented to provide an angularly resolved measurement of the SRS emission spectrum: Angular-Resolved Scattered-light Diagnostic Station (ARSDS) [24]. It enabled to observe broadband SRS light emitted over a wide spatial area. Direct comparison with the back-scattered light collected in the aperture of one of the driver beam evidenced SRSS as the dominant SRS process. 2D PIC simulations confirmed that in this regime, the interaction was below the threshold for the typical SRBS to grow and only SRSS was responsible for the SRS emission. Due to its broad spatial emission, SRSS was identified to be responsible for the scattering of up to $5 \pm 2\%$ of the total laser energy and requires to be measured over the whole interaction volume.

The experiment was performed at the SG-II UP laser facility [25] using the setup displayed on Fig. 1(a). For clarity, we define here that beam #7 azimuthal position is the origin $\varphi = 0^\circ$ of the azimuth axis and that the north pole is the origin $\theta = 0^\circ$ of the polar axis. A cone of four beams were used to irradiate a 45 μm-thick CH spherical cap target, with an inner radius of 450 μm. The CH cap is contained within a 20 μm-thick, open-ended Au cone. The cone of four beams, #1, #3, #5 and #7, were incident on the CH target at a polar angle of $\theta = 50^\circ$, uni-

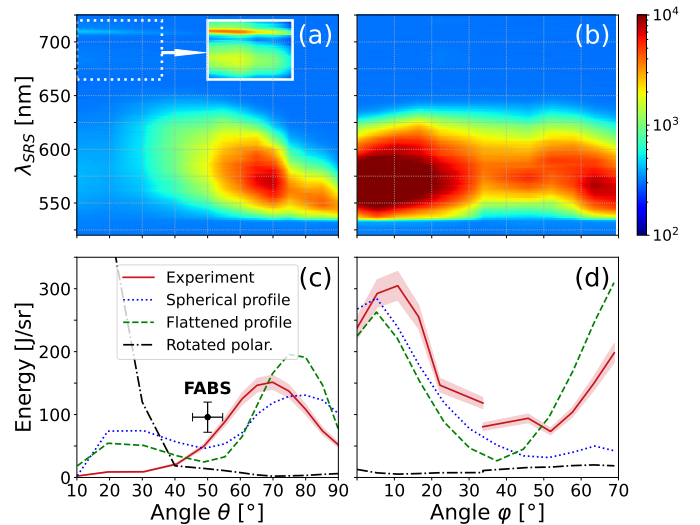


Figure 2. Typical ARSDS spectrum of the SRS emission against (a) the polar angle collected at an azimuthal angle of 33.7° ; (b) the azimuthal angle collected at polar angles displayed in Fig. 1(c). The inset in (a) presents the contrast enhanced TPD features. (c) (resp. (d)) Red plain line is the scattered energy against the exit angle, integrated over the spectrum (a) (resp. (b)) and normalized to the collection solid angle. Back-scattered energy measured by FABS is displayed as a black dot on (c). The discontinuity in (d) is due to the different polar coordinate, as shown in Fig. 1(c). On (c) and (d), blue dotted, green dashed and black dash-dot lines present the scattered light signal in arbitrary units from the ray-tracing simulations with respectively ideal spherical compression, flattened compression and rotated polarization.

formly distributed in the azimuthal direction. The beams are primarily p-polarised plus an angle of 7° for beams #3, #5 and 23° for beams #1, #7. Each beam delivers 1.5 kJ at 351 nm focused by a $f/7.1$ wedged lens on target within a $525 \mu\text{m}$ ($1/e^2$), CPP smoothed focal spot, with a pulse shape presented on Fig. 1(b), reaching a peak overlapped intensity of $\approx 1.8 \times 10^{15} \text{ W.cm}^{-2}$ in vacuum. At peak power, plasma parameters were estimated using the hydro-radiative code MULTI2D [26], predicting a density scale-length of $L_{n_c/4} \approx 200 \mu\text{m}$ at $n_c/4$ up to $L_{n_c/10} \approx 250 \mu\text{m}$ in the coronal plasma, with a uniform electron temperature from $T_e \approx 2.0$ to 2.5 keV. The electron temperature near $n_c/4$ was confirmed to be ≤ 2.2 keV from the red shifted-spectral feature related to Two-Plasmon Decay (TPD) instability [27], as shown by the inset in Fig. 2(a). A Full-Aperture Back-scattering Station (FABS) was installed on #7 in order to collect the light scattered in the backward direction $[\theta, \varphi] = [50^\circ, 0^\circ]$. ARSDS was used to collect the SRS scattered light in both azimuthal and polar axes, at the coordinates depicted by the black dots in Fig. 1(c), in order to obtain temporally integrated spectra resolved in angle.

A typical result is presented on Fig. 2, displaying the

scattered light spectrum angularly resolved in the (a) polar and (b) azimuthal directions. The overall signal is dominated by light with a spectrum ranging from 540 nm up to 640 nm emitted within a wide area ranging from 30° up to 90° polar angles, over the whole azimuth, corresponding to a density range of $\approx [0.1 - 0.2]n_c$. The plain red curve on Fig. 2(c) (resp. Fig. 2(d)) presents the signal from Fig. 2(a) (resp. Fig. 2(b)) integrated over the spectrum, calibrated in energy and normalised to the solid angle. It shows that most of the scattered light is emitted at large polar angles, peaked around $\theta = 70^\circ$. Such signal corresponds to an SRS emission at shorter wavelength and larger angle than previously reported, where usually the detection of SRS light is limited to angles $\leq 50^\circ$. Furthermore, Fig. 2(d) shows that the amount of scattered energy is sensitive to the azimuthal position. The maximum emission is not contained in the azimuthal plane of the laser beam but is offset by an angle $\Delta\varphi \approx 10^\circ$.

Considering that the broadband signal is emitted at polar angles larger than the incident driver beams, over a large azimuthal section, it evidences that side-scattering is responsible for such emission. The SRSS scattered light is emitted orthogonal to the density gradient and experiences refraction on its way out of the plasma [15, 20]. This results in a correlation between the scattered light wavelength and the polar exit angle, as observed on Fig. 2(a). Moreover, SRSS scattered light is also emitted perpendicular to the laser polarization plane, as reported in theoretical [2, 15, 28] and numerical [29–31] studies. Considering the 2D spherical nature of our target, the inherent sensitivity of SRSS to the plasma profile and laser polarization, numerical simulations are required to confirm the observed angular spread of the scattered light. A new 3D ray-tracing code PHANTAM [32], based on the method published by Kaiser [33], has been developed to simulate the propagation of the SRSS light, also accounting for collisional absorption. The simulation box is $0.4\text{cm} \times 0.4\text{cm} \times 0.3\text{cm}$ with a $200 \times 200 \times 300$ mesh, containing a plasma obtained from the hydrodynamic simulations. SRSS light is generated when incident rays propagate into the the electron density range $[0.12, 0.20]n_c$, at the associated wavelength, consistent with the experimental data, without gain or threshold consideration. SRSS rays are initialized perpendicular to both the local density gradient and the local polarization of the incident ray with a 9-degree random spreading angle. Upon exiting the plasma, SRSS rays are collected at the same positions than ARSDS detectors. As displayed by the blue dotted curves in Fig. 2(c) and (d), such simulations are confirming an emission at large polar angles, maximized near the beam azimuth, despite several discrepancies. These are likely the result of difference in plasma profiles between the ideal spherical compression from the simulation [34] and the actual experiment. This assumption can be confirmed by reducing the discrepancies when

considering a plasma profile flattened along the target normal, as depicted by the green dashed curves in Fig. 2(c) and (d). The importance of the laser polarization is highlighted by the black dash-dot curves, showing a completely different scattering profile when the polarization of each beam is rotated by 90° . These simulations show that the scattering is a complex combination of plasma profile, polarization and single-beam contribution from beam #7 and the neighbour beam #5. Further investigations, beyond the scope of this paper, are necessary to improve numerical agreement with the experiment and will be the subject of future work.

From these spectra, it appears that the scattering is driven by single beam SRSS, as multi-beam process would drive scattered light either in the bisector plan at $\varphi \approx 45^\circ$ for a shared scattered electromagnetic wave [16, 17], or constrained to density $n_e \leq 0.12n_c$ for a shared EPW due to the large angle between two neighbouring beams [19]. This was further confirmed by experimentally measuring a two-orders-of-magnitude decrease of the signal in the polar direction when #7 is switched off, and retrieving the overall emission profile in the ray-tracing simulations from independent beam contribution. Thus, single-beam intensity is considered in the following discussion.

In ICF experiments, SRSS can experience both absolute or convective growth, depending on the interaction conditions. Figure 3 presents SRSS convective gain [20] and absolute threshold [15] against the scattered light wavelength and incident laser intensity, for our conditions considering oblique incidence and damping. It appears that the absolute threshold is overcome for most of the density range. The lower density part can be interpreted considering the convective regime, having a moderate gain in our intensity range, where the white curve highlights the iso-contour corresponding to a gain of 1. The absence of signal above 640 nm in our data is likely due to the significant re-absorption at the associated high density, as previously reported [16, 20]. At low density, Michel [20] reported that the finite size of the beam is limiting the convective growth of SRSS, which requires a large transverse amplification length. Considering a $525 \mu\text{m}$ focal spot, this corresponds to a cutoff around 530 nm in our conditions, consistent with our experimental observations.

FABS measurements typically show a slightly higher amount of scattered energy than ARSDS (≈ 1.5 higher), with similar spectrum, for the same polar angle as shown on the Fig. 2(c), despite the difference in azimuth, consistent with Fig. 2(d). Such measurement evidences that there is no stronger emission localised in the backward direction which could be attributed to SRBS. This is expected as the laser intensity is one order of magnitude lower than the predicted SRBS threshold of $\approx 4.5 \times 10^{15} \text{ W.cm}^{-2}$ for our conditions [2, 5, 35]. Such low laser intensity also prevents SRBS to grow from the

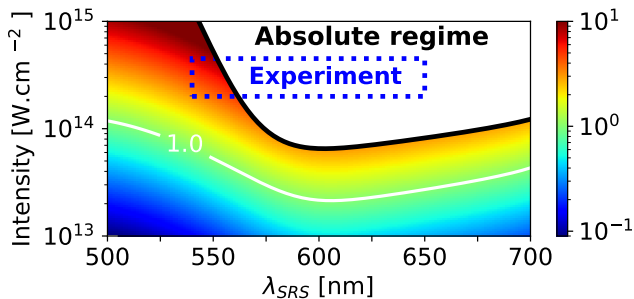


Figure 3. SRSS convective gain against laser intensity and scattered light wavelength, for our experimental plasma conditions $L_{n_c/10} \approx 250 \mu\text{m}$ and $T_e = 2.0 \text{ keV}$. The white curve highlights the iso-contour corresponding to a gain of 1. The white region corresponds to the absolute regime. The dashed blue rectangle highlights our experimental measurements.

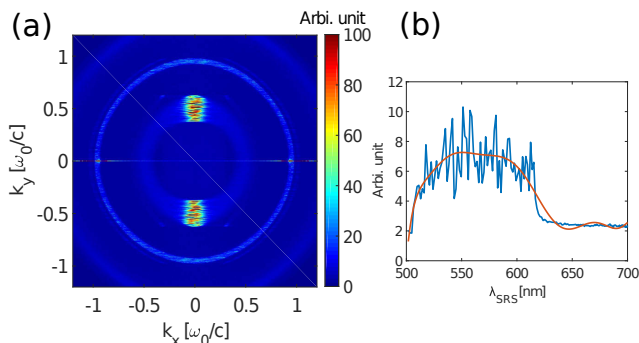


Figure 4. (a) 2D spectrum of the scattered light averaged over 2 ps, (b) and associated spectrum from PIC simulations.

high intensity speckles [36, 37], which have been inferred to reach up to $\approx 2.5 \times 10^{15} \text{ W.cm}^{-2}$. This results in a negligible reflectivity measured by FABS, $\leq 0.15 \pm 0.05\%$, as being only a fraction of the total scattered energy. In order to account for the large scattering angular spread, 50 additional fibers [38] were used along with ARSDS and FABS in order to extend the spatial measurement over $\frac{4}{3}\pi$, as depicted on Fig. 1(c). This diagnostic setup is similar to ARSDS, providing an energy measurement of SRS scattering integrated in time. Despite inherent uncertainties due to the limited number of directions probed, a reflectivity up to $5 \pm 2\%$ of the total laser energy was estimated, without considering the absorption. This evidences that SRSS is energetically significant and necessitates to be measured over the whole interaction volume. This implies that SRSS can lead to additional losses not usually accounted for and could be one candidate to explain some “missing” energy reported in recent experiments [6, 39]. Indeed, it appears that SRSS losses can be easily overlooked as only scattering a low amount of energy locally, which would normally not be detected or considered.

To confirm the predominance of SRSS over SRBS, 2D

plane-wave PIC simulations have been performed using the code EPOCH [40]. An s-polarized plane wave is normally incident into a linear-density-profile plasma slab ranging from $0.1n_c$ to $0.2n_c$, with a density scale-length of $250 \mu\text{m}$. The full simulation box is $200 \mu\text{m}$ in length (x-axis) and $80 \mu\text{m}$ in width (y-axis), and there is a $10 \mu\text{m}$ vacuum at the left boundary. The longitudinal boundary conditions are open boundary for fields and thermal boundary for particles, and the transverse boundary condition is periodic. Interaction parameters are as follow: the laser intensity $I_0 = 4.5 \times 10^{14} \text{ W.cm}^{-2}$, the electron temperature $T_e = 2 \text{ keV}$, and fixed ions. Figure 4(a) shows a time-averaged 2D spectrum of the scattered light wave over 2 ps. The brightest signals are the near 90° scattered light perpendicular to the density gradient. As expected, there is no measurable SRBS due to its negligible convective gain. Figure 4(b) shows the scattered light spectrum confirming SRSS growth over the whole range of density simulated, consistent with the experiment.

In conclusion, it was experimentally evidenced and confirmed by 2D PIC simulations that side-scattering is the dominant stimulated Raman scattering geometry in the compression stage of DCI experiment. Due to the sensitivity to both plasma profile and laser polarization, SRSS scattered light is emitted over a wide volume, as observed experimentally and confirmed by ray-tracing simulations. Such broad angular scattering results in a small amount of energy being scattered locally, while being energetically significant when measured over the whole interaction volume. Thus, relying on limited directions to diagnose SRS, such as back-scattering, could lead to a strong underestimation of the actual energy losses, by a factor of 35 in our conditions. Even though the results discussed here were obtained using conical targets, it was verified experimentally that our conclusions were still valid for planar targets. Thus, the importance and relevance of our observations can be extended beyond the DCI scheme. However, to assess the impact and significance of side-scattering on other ICF schemes, further investigations are required such as: (i) SRSS behavior at higher intensities; (ii) the competition between Raman side- and back-scattering when SRBS threshold is overcome; (iii) the effect of laser smoothing techniques such as smoothing by spectral dispersion (SSD) [41] which could reportedly mitigate SRSS [42].

We thank the SG-II UP operating group and target fabrication team for their assistance. This work was supported by the Strategic Priority Research Program of Chinese Academy of Sciences (grants No. XDA25010100, No. XDA25030200 & No. XDA25050700).

* These two authors contributed equally

- [†] Authors to whom correspondence should be addressed
xiaoahui.yuan@sjtu.edu.cn and jzhang1@sjtu.edu.cn
- [1] J. Nuckolls, L. Wood, A. Thiessen, and G. Zimmeran, *Nature* **239**, 139 (1972).
 - [2] W. L. Kruer, *Journal of Plasma Physics* **45**, 135 (1991).
 - [3] G. G. Comisar, *Phys. Rev.* **141**, 200 (1966).
 - [4] R. K. Kirkwood, J. D. Moody, J. Kline, E. Dewald, S. Glenzer, L. Divol, P. Michel, D. Hinkel, R. Berger, E. Williams, J. Milovich, L. Yin, H. Rose, B. MacGowan, O. Landen, M. Rosen, and J. Lindl, *Plasma Physics and Controlled Fusion* **55**, 103001 (2013).
 - [5] D. S. Montgomery, *Physics of Plasmas* **23**, 055601 (2016), <https://doi.org/10.1063/1.4946016>.
 - [6] G. N. Hall, O. S. Jones, D. J. Strozzi, J. D. Moody, D. Turnbull, J. Ralph, P. A. Michel, M. Hohenberger, A. S. Moore, O. L. Landen, L. Divol, D. K. Bradley, D. E. Hinkel, A. J. Mackinnon, R. P. J. Town, N. B. Meezan, L. Berzak Hopkins, and N. Izumi, *Physics of Plasmas* **24**, 052706 (2017).
 - [7] M. J. Rosenberg, A. A. Solodov, J. F. Myatt, W. Seka, P. Michel, M. Hohenberger, R. W. Short, R. Epstein, S. P. Regan, E. M. Campbell, T. Chapman, C. Goyon, J. E. Ralph, M. A. Barrios, J. D. Moody, and J. W. Bates, *Phys. Rev. Lett.* **120**, 055001 (2018).
 - [8] M. J. Rosenberg, A. A. Solodov, W. Seka, R. K. Follett, J. F. Myatt, A. V. Maximov, C. Ren, S. Cao, P. Michel, M. Hohenberger, J. P. Palastro, C. Goyon, T. Chapman, J. E. Ralph, J. D. Moody, R. H. H. Scott, K. Glize, and S. P. Regan, *Physics of Plasmas* **27**, 042705 (2020), <https://doi.org/10.1063/1.5139226>.
 - [9] R. H. H. Scott, K. Glize, L. Antonelli, M. Khan, W. Theobald, M. Wei, R. Betti, C. Stoeckl, A. G. Seaton, T. D. Arber, D. Barlow, T. Goffrey, K. Bennett, W. Garbett, S. Atzeni, A. Casner, D. Batani, C. Li, and N. Woolsey, *Phys. Rev. Lett.* **127**, 065001 (2021).
 - [10] G. Cristoforetti, L. Antonelli, D. Mancelli, S. Atzeni, F. Baffigi, F. Barbato, D. Batani, G. Boutoux, F. D'Amato, J. Dostal, R. Dudzak, E. Filippov, Y. J. Gu, L. Juha, O. Klimo, M. Krus, S. Malko, A. S. Martynenko, P. Nicolai, V. Ospina, S. Pikuz, O. Renner, J. Santos, V. T. Tikhonchuk, J. Trela, S. Viciani, L. Volpe, S. Weber, and L. A. Gizzi, *High Power Laser Science and Engineering* **7** (2019), 10.1017/hpl.2019.37.
 - [11] G. Cristoforetti, S. Hüller, P. Koester, L. Antonelli, S. Atzeni, F. Baffigi, D. Batani, C. Baird, N. Booth, M. Galimberti, K. Glize, A. Héron, M. Khan, P. Loiseau, D. Mancelli, M. Notley, P. Oliveira, O. Renner, M. Smid, A. Schiavi, G. Tran, N. C. Woolsey, and L. A. Gizzi, *High Power Laser Science and Engineering* **9**, e60 (2021).
 - [12] S. Baton, A. Colaitis, C. Rousseaux, G. Boutoux, S. Brygoo, L. Jacquet, M. Koenig, D. Batani, A. Casner, E. L. Bel, D. Raffestin, A. Tentori, V. Tikhonchuk, J. Trela, C. Reverdin, L. Le-Deroff, W. Theobald, G. Cristoforetti, L. Gizzi, P. Koester, L. Labate, and K. Shigemori, *High Energy Density Physics* **36**, 100796 (2020).
 - [13] C. S. Liu, M. N. Rosenbluth, and R. B. White, *The Physics of Fluids* **17**, 1211 (1974), <https://aip.scitation.org/doi/pdf/10.1063/1.1694867>.
 - [14] M. A. Mostrom and A. N. Kaufman, *Phys. Rev. Lett.* **42**, 644 (1979).
 - [15] B. B. Afeyan and E. A. Williams, *The Physics of Fluids* **28**, 3397 (1985), <https://aip.scitation.org/doi/pdf/10.1063/1.865340>.
 - [16] S. Depierreux, C. Neuville, C. Baccou, V. Tassin, M. Casanova, P.-E. Masson-Laborde, N. Borisenko, A. Orekhov, A. Colaitis, A. Debayle, G. Duchateau, A. Heron, S. Huller, P. Loiseau, P. Nicolai, D. Pesme, C. Riconda, G. Tran, R. Bahr, J. Katz, C. Stoeckl, W. Seka, V. Tikhonchuk, and C. Labaune, *Phys. Rev. Lett.* **117**, 235002 (2016).
 - [17] S. Depierreux, C. Neuville, V. Tassin, M.-C. Monteil, P.-E. Masson-Laborde, C. Baccou, P. Fremerye, F. Philippe, P. Seytor, D. Teychenné, J. Katz, R. Bahr, M. Casanova, N. Borisenko, L. Borisenko, A. Orekhov, A. Colaitis, A. Debayle, G. Duchateau, A. Heron, S. Huller, P. Loiseau, P. Nicolai, C. Riconda, G. Tran, C. Stoeckl, W. Seka, V. Tikhonchuk, D. Pesme, and C. Labaune, *Plasma Physics and Controlled Fusion* **62**, 014024 (2019).
 - [18] R. W. Short, *Physics of Plasmas* **27**, 042703 (2020), <https://doi.org/10.1063/1.5131158>.
 - [19] P. Michel, L. Divol, E. L. Dewald, J. L. Milovich, M. Hohenberger, O. S. Jones, L. B. Hopkins, R. L. Berger, W. L. Kruer, and J. D. Moody, *Phys. Rev. Lett.* **115**, 055003 (2015).
 - [20] P. Michel, M. J. Rosenberg, W. Seka, A. A. Solodov, R. W. Short, T. Chapman, C. Goyon, N. Lemos, M. Hohenberger, J. D. Moody, S. P. Regan, and J. F. Myatt, *Phys. Rev. E* **99**, 033203 (2019).
 - [21] M. J. Rosenberg, J. E. Hernandez, N. Butler, T. Filkins, R. E. Bahr, R. K. Jungquist, M. Bedzyk, G. Swadling, J. S. Ross, P. Michel, N. Lemos, J. Eichmiller, R. Sommers, P. Nyholm, R. Boni, J. A. Marozas, R. S. Craxton, P. W. McKenty, A. Sharma, P. B. Radha, D. H. Froula, P. Datte, M. Gorman, J. D. Moody, J. M. Heimmler, J. Fornes, P. Hillyard, and S. P. Regan, *Review of Scientific Instruments* **92**, 033511 (2021), <https://doi.org/10.1063/5.0040558>.
 - [22] J. Zhang, W. M. Wang, X. H. Yang, D. Wu, Y. Y. Ma, J. L. Jiao, Z. Zhang, F. Y. Wu, X. H. Yuan, Y. T. Li, and J. Q. Zhu, *Philosophical Transactions of the Royal Society A: Mathematical, Physical and Engineering Sciences* **378**, 20200015 (2020), <https://doi.org/10.1098/rsta.2020.0015>.
 - [23] R. L. McCrory, D. D. Meyerhofer, R. Betti, R. S. Craxton, J. A. Delettrez, D. H. Edgell, V. Y. Glebov, V. N. Goncharov, D. R. Harding, D. W. Jacobs-Perkins, J. P. Knauer, F. J. Marshall, P. W. McKenty, P. B. Radha, S. P. Regan, T. C. Sangster, W. Seka, R. W. Short, S. Skupsky, V. A. Smalyuk, J. M. Soures, C. Stoeckl, B. Yaakobi, D. Shvarts, J. A. Frenje, C. K. Li, R. D. Petrasso, and F. H. Séguin, *Physics of Plasmas* **15**, 055503 (2008), <https://doi.org/10.1063/1.2837048>.
 - [24] X. Zhao, X. H. Yuan, J. Zheng, Y. F. Dong, K. Glize, Y. H. Zhang, Z. Zhang, and J. Zhang, *Review of Scientific Instruments* **93**, 053505 (2022), <https://doi.org/10.1063/5.0090841>.
 - [25] G. Xu, T. Wang, Z. Li, Y. Dai, Z. Lin, Y. Gu, and J. Zhu, *The Review of Laser Engineering* **36**, 1172 (2008).
 - [26] R. Ramis, J. M. ter Vehn, and J. Ramírez, *Computer Physics Communications* **180**, 977 (2009).
 - [27] W. Seka, B. B. Afeyan, R. Boni, L. M. Goldman, R. W. Short, K. Tanaka, and T. W. Johnston, *The Physics of Fluids* **28**, 2570 (1985), <https://aip.scitation.org/doi/pdf/10.1063/1.865265>.
 - [28] C. R. Menyuk, N. M. El-Siragy, and W. M. Manheimer, *The Physics of Fluids* **28**, 3409 (1985), <https://aip.scitation.org/doi/pdf/10.1063/1.865341>.

- [29] C. Z. Xiao, Z. J. Liu, C. Y. Zheng, and X. T. He, *Physics of Plasmas* **23**, 022704 (2016), <https://doi.org/10.1063/1.4941969>.
- [30] C. Z. Xiao, H. B. Zhuo, Y. Yin, Z. J. Liu, C. Y. Zheng, Y. Zhao, and X. T. He, *Plasma Physics and Controlled Fusion* **60**, 025020 (2018).
- [31] Y.-J. Gu, O. Klimo, V. Tikhonchuk, and S. Weber, *Nuclear Fusion* **61**, 066014 (2021).
- [32] Y. Ji, C. W. Lian, and R. Yan, **in preparation** (2022).
- [33] T. B. Kaiser, *Phys. Rev. E* **61**, 895 (2000).
- [34] M. Yang, F. Y. Wu, Z. B. Chen, Y. X. Zhang, Y. Chen, J. C. Zhang, Z. Z. Chen, Z. F. Fang, R. Ramis, and J. Zhang, *Acta Physica Sinica* **submitted** (2022).
- [35] K. Estabrook and W. L. Kruer, *The Physics of Fluids* **26**, 1892 (1983), <https://aip.scitation.org/doi/pdf/10.1063/1.864336>.
- [36] C. Rousseaux, K. Glize, S. D. Baton, L. Lancia, D. Bénisti, and L. Gremillet, *Phys. Rev. Lett.* **117**, 015002 (2016).
- [37] K. Glize, C. Rousseaux, D. Bénisti, V. Dervieux, L. Gremillet, S. D. Baton, and L. Lancia, *Physics of Plasmas* **24**, 032708 (2017), <https://doi.org/10.1063/1.4978879>.
- [38] Y. H. Zhang, *Review of Scientific Instruments* **in preparation** (2022).
- [39] D. Turnbull, J. Katz, D. E. Hinkel, P. Michel, T. Chapman, L. Divol, E. Kur, S. MacLaren, A. L. Milder, M. Rosen, A. Shvydky, G. B. Zimmerman, and D. H. Froula, *Phys. Rev. Lett.* **129**, 025001 (2022).
- [40] T. D. Arber, K. Bennett, C. S. Brady, A. Lawrence-Douglas, M. G. Ramsay, N. J. Sircombe, P. Gillies, R. G. Evans, H. Schmitz, A. R. Bell, and C. P. Ridgers, *Plasma Physics and Controlled Fusion* **57**, 113001 (2015).
- [41] S. Skupsky, R. W. Short, T. Kessler, R. S. Craxton, S. Letzring, and J. M. Soures, *Journal of Applied Physics* **66**, 3456 (1989), <https://doi.org/10.1063/1.344101>.
- [42] N. Kang, H. Liu, S. Zhou, Y. Zhao, and A. Lei, *J. Opt. Soc. Am. B* **38**, 3567 (2021).